Harmonic State-Space Based Small-Signal Impedance Modeling of a Modular Multilevel Converter With Consideration of Internal Harmonic Dynamics

Jing Lyu, *Member, IEEE*, Xin Zhang, *Member, IEEE*, Xu Cai, and Marta Molinas, *Member, IEEE*

***Abstract*—The small-signal impedance modeling of a modular multilevel converter (MMC) is the key for analyzing resonance and stability of MMC-based power electronic systems. The MMC is a power converter with a multifrequency response due to its significant steady-state harmonic components in the arm currents and capacitor voltages. These internal harmonic dynamics may have great influence on the terminal characteristics of the MMC, which, therefore, are essential to be considered in the MMC impedance modeling. In this paper, the harmonic state-space (HSS) modeling approach is first introduced to characterize the multiharmonic coupling behavior of the MMC. On this basis, the small-signal impedance models of the MMC are then developed based on the proposed HSS model of the MMC, which are able to include all the internal harmonics within the MMC, leading to accurate impedance models. Besides, different control schemes for the MMC, such as open-loop control, ac voltage closed-loop control, and circulating current closed-loop control, have also been considered during the modeling process, which further reveals the impact of the MMC internal dynamics and control dynamics on the MMC impedance. Furthermore, an impedance-based stability analysis of the MMC-high-voltage direct current connected wind farm has been carried out to show how the HSS-based MMC impedance model can be used in practical system analysis. Finally, the proposed impedance models are validated by both simulation and experimental measurements.**

Manuscript received January 19, 2017; revised April 18, 2018; accepted May 22, 2018. Date of publication May 30, 2018; date of current version February 5, 2019. This work was supported in part by the National Key Research and Development Program under Grant 2016YFB0900901, in part by the Shanghai Science and Technology Committee Scientific Research Program under Grant 16DZ1203402, and in part by the Key Laboratory of Control of Power Transmission and Conversion of Ministry of Education under Grant 2016AC05. Recommended for publication by Associate Editor M. Ordonez. *(Corresponding author: Xu Cai.)*

J. Lyu was with the Department of Engineering Cybernetics, Norwegian University of Science and Technology, Trondheim 7491, Norway. He is now with the Wind Power Research Center, School of Electronic Information and Electrical Engineering, Shanghai Jiao Tong University, Shanghai 200240, China (e-mail:

extended to any number of harmonics. What is more, the MMC models in the time periodic framework were derived in [16] and [17], which can achieve high accuracy, but still need lengthy algebra and are difficult to be used for harmonic interaction and stability analysis in power electronics interconnected systems.

Fortunately, the harmonic state-space (HSS) modeling method [18]–[26] can overcome the above-mentioned limitations. The HSS modeling is able to simultaneously represent multiple frequency responses in each variable and to build multidimensional harmonic transfer function based models [23]. Furthermore, the HSS model, in which harmonics of state variables, inputs, and outputs are posed separately in a state-space form, is easy to be implemented by a computer (e.g., MATLAB) and to be extended to any number of harmonics. The HSS method has already been used in many fields of power systems, e.g., buck–boost converter [20], thyristor-controlled reactor [21], single- and three-phase two-level VSCs [22]–[26], MMC [27], etc.

The impedance-based stability analysis method is one of the preferred methods for stability analysis of power electronic systems, especially for multiconverter interconnected systems [28], [29]. The impedance modeling of power converters is the prerequisite for applying the impedance-based analytical approach. Most of the research has so far focused on the impedance modeling of two-level converters [30]–[32], while only a number of researchers have reported the impedance modeling of the MMC. The dc-side impedance [33], [34] and ac-side impedance [35], [36] of the MMC were derived, respectively, where, however, the submodule (SM) capacitors are assumed to be large enough and the internal harmonic dynamics are neglected, which are usually improper in practice. A few papers discussed the MMC impedance modeling with consideration of internal harmonics [37]–[39]. In [37], the harmonic linearization method was directly applied to derive the MMC impedance, in which, however, the algebraic operation is lengthy, particularly serious if higher harmonics are considered. The HSS method was also introduced by the authors to develop the impedance model of the MMC in [38]. In addition, a new method called multiharmonic linearization, which is essentially equivalent to the HSS method, was proposed to derive the sequence impedance of the MMC in [39]. What distinguishes this paper from the above-mentioned contributions is that the impact of the internal harmonics and circulating current control on the MMC impedance is analyzed and experimental measurements are also provided to further validate the proposed impedance models.

The paper is organized as follows. The formulation of the HSS modeling is reviewed, and the large- and small-signal HSS models of the MMC are then presented in Section II. In Section III, the small-signal impedance of the MMC is derived based on the developed HSS model. As a case study, an impedance-based stability analysis of the MMC-HVDC-connected wind farm has been carried out to show how the proposed impedance model is used in practical system analysis in Section IV. The simulation and experimental results are provided to validate the proposed MMC impedance models in Section V. Section VI concludes the paper.

II. HSS-Based Large/Small-Signal Models of the MMC

A. Preliminary and Formulation of HSS Modeling

For any time-varying periodic signal $x(t)$, it can be written in the form of the Fourier series as

$$x\left(t\right)=\sum_{k\in\mathbb{Z}}X_k e^{jk\omega_1 t} \tag{1}$$

where $\omega_1=2\pi/T, T$ is the fundamental period of the signal, and X_k is the Fourier coefficient that can be calculated by

$$X_k=\frac{1}{T}\int_{t_0}^{t_0+T}x\left(t\right)e^{-jk\omega_1 t}dt. \tag{2}$$

The time-domain state-space equation of the studied system can be expressed as [18]–[27]

$$\dot{x}(t)=A(t)x(t)+B(t)u(t). \tag{3}$$

Based on the Fourier series and harmonic balance theory [18], the time-domain state-space equation can be transformed into the frequency-domain HSS equation, which is [20]–[27]

$$s\mathbf{X}=(\mathbf{A}-\mathbf{Q})\mathbf{X}+\mathbf{B}\mathbf{U} \tag{4}$$

where **X**, **U**, **A**, **B**, and **Q** are indicated as (5)–(9), respectively, of which the elements X_h, U_h, A_h, and B_h are the Fourier coefficients of the hth harmonic of $x(t), u(t), A(t)$, and $B(t)$ in (3), respectively. Note that **A** and **B** are Toeplitz matrices in order to perform the frequency-domain convolution operation, **Q** is a diagonal matrix that represents the frequency information, and I is an identity matrix having the same matrix size with the number of state variables. In addition, h is the harmonic order considered in the model

$$\mathbf{X}=[X_{-h},\ldots,X_{-1},X_0,X_1,\ldots,X_h]^T \tag{5}$$

$$\mathbf{U}=[U_{-h},\ldots,U_{-1},U_0,U_1,\ldots,U_h]^T \tag{6}$$

$$\mathbf{A}=\begin{bmatrix} A_0 & A_{-1} & \cdots & A_{-h} & & & \\ A_1 & \ddots & \ddots & \ddots & \ddots & & \\ \vdots & \ddots & A_0 & A_{-1} & \ddots & \ddots & \\ A_h & \ddots & A_1 & A_0 & A_{-1} & \ddots & A_{-h} \\ & \ddots & \ddots & A_1 & A_0 & \ddots & \vdots \\ & & \ddots & \ddots & \ddots & \ddots & A_{-1} \\ & & & A_h & \cdots & A_1 & A_0 \end{bmatrix} \tag{7}$$

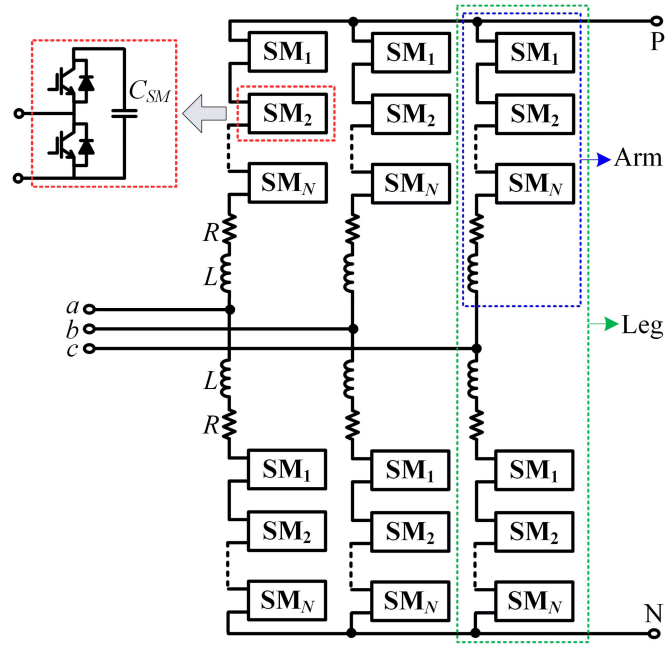

Fig. 1. Circuit diagram of a three-phase MMC.

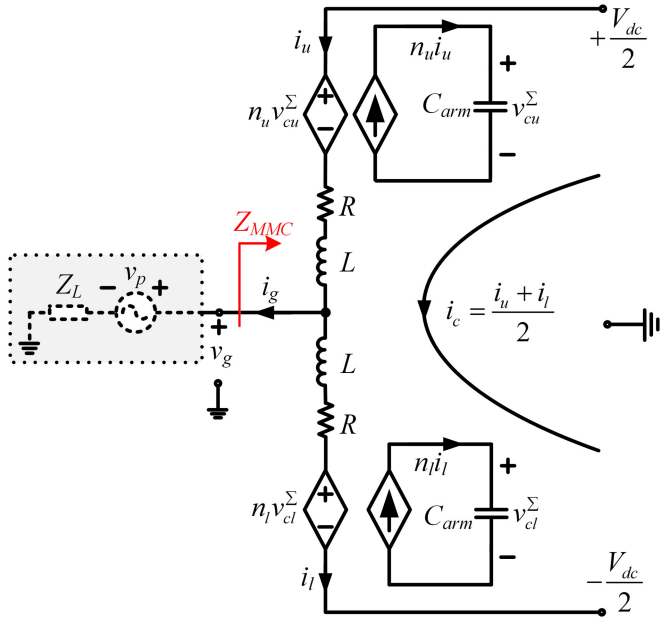

Fig. 2. Averaged equivalent circuit of one phase leg of the MMC.

$$\mathbf{B} = \begin{bmatrix} B_0 & B_{-1} & \cdots & B_{-h} & & & \\ B_1 & \ddots & \ddots & \ddots & \ddots & & \\ \vdots & \ddots & B_0 & B_{-1} & \ddots & \ddots & \\ B_h & \ddots & B_1 & B_0 & B_{-1} & \ddots & B_{-h} \\ & \ddots & \ddots & B_1 & B_0 & \ddots & \vdots \\ & & \ddots & \ddots & \ddots & \ddots & B_{-1} \\ & & & B_h & \cdots & B_1 & B_0 \end{bmatrix} \tag{8}$$

$$\mathbf{Q} = \begin{bmatrix} -jh\omega_1 \cdot I & & & & \\ & \ddots & & & \\ & & 0 \cdot I & & \\ & & & \ddots & \\ & & & & jh\omega_1 \cdot I \end{bmatrix}. \tag{9}$$

B. HSS-Based Large-Signal Model of the MMC

Fig. 1 shows the circuit diagram of a three-phase MMC. Each phase-leg of the MMC consists of one upper and one lower arm connected in series between the dc terminals. Each arm consists of N identical series-connected SMs, one arm inductor L, and its equivalent series resistor R. Each SM contains a half-bridge as a switching element and a dc storage capacitor $C_{\rm SM}$. In high-voltage applications, N may be as high as several hundreds. It should be noted that the SM may use a half-bridge or a full-bridge topology, which, however, does not affect the discussion here. Moreover, it needs to be pointed out that the modulation and voltage-balancing control have little effects on the impedance response due to their action on a cycle-by-cycle at the switching frequency.

It is assumed that the equivalent switching frequency is high enough and the capacitor voltages are balanced at all times [3], [4]. This way the need for treating the SMs individually can be avoided and each arm can be treated as one equivalent SM. Hence, according to the average-value modeling method [9], the averaged equivalent circuit of the MMC can be obtained, as presented in Fig. 2 (taking one phase, for example), where $C_{\rm arm} = C_{\rm SM}/N, i_u(t)$ and $i_l(t)$ are the upper and lower arm currents, $v_{cu}^{\Sigma}(t)$ and $v_{cl}^{\Sigma}(t)$ are the sum capacitor voltages of the upper and lower arms, $v_g(t)$ and $i_g(t)$ are the ac-side phase voltage and current, $i_c(t)$ is the circulating current, $V_{\rm dc}$ is the dc bus voltage, and $n_u(t)$ and $n_l(t)$ are the switching functions of the upper and lower arms. In addition, $Z_L(= R_L + j\omega_1 L_L)$ is the ac-side equivalent load in order to determine the steady-state operating point, and $v_p(t)$ is the injected small perturbation voltage in order to derive the small-signal impedance of the MMC according to the harmonic linearization theory. Furthermore, the dc-link voltage $V_{\rm dc}$ is assumed to be constant.

The circulating current is defined as

$$i_c(t) = \frac{i_u(t) + i_l(t)}{2}. \tag{10}$$

The ac phase current can be expressed as

$$i_g(t) = i_u(t) - i_l(t). \tag{11}$$

Applying Kirchhoff's law to the single-phase equivalent circuit of the MMC shown in Fig. 2, one can obtain

$$v_g(t) + L\frac{di_u(t)}{dt} + Ri_u(t) + v_u(t) = \frac{V_{\rm dc}}{2} \tag{12}$$

$$v_g(t) - L\frac{di_l(t)}{dt} - Ri_l(t) - v_l(t) = -\frac{V_{\rm dc}}{2}. \tag{13}$$

Based on the continuous model of the MMC [3], [4], we have

$$\begin{cases} v_u(t) = n_u(t) v_{cu}^{\sum}(t) \\ v_l(t) = n_l(t) v_{cl}^{\sum}(t) \end{cases} \tag{14}$$

$$\begin{cases} C_{\rm arm} \frac{dv_{cu}^{\sum}(t)}{dt} = n_u(t) i_u(t) \\ C_{\rm arm} \frac{dv_{cl}^{\sum}(t)}{dt} = n_l(t) i_l(t). \end{cases} \tag{15}$$

Substituting $v_g = Z_L i_g$ into (12) and (13), (10)–(15) can be reorganized into the state-space form as (3), where $x(t), u(t), A(t)$, and $B(t)$ are given as

$$x(t) = \left[i_c(t), v_{cu}^{\sum}(t), v_{cl}^{\sum}(t), i_g(t) \right]^T \tag{16}$$

$$u(t) = [V_{\rm dc}] \tag{17}$$

$$A(t) = \begin{bmatrix} -\frac{R}{L} & -\frac{n_u(t)}{2L} & -\frac{n_l(t)}{2L} & 0 \\ \frac{n_u(t)}{C_{\rm arm}} & 0 & 0 & \frac{n_u(t)}{2C_{\rm arm}} \\ \frac{n_l(t)}{C_{\rm arm}} & 0 & 0 & -\frac{n_l(t)}{2C_{\rm arm}} \\ 0 & -\frac{n_u(t)}{L} & \frac{n_l(t)}{L} & -\frac{R+2Z_L}{L} \end{bmatrix} \tag{18}$$

$$B(t) = \left[\frac{1}{2L}, 0, 0, 0 \right]^T \tag{19}$$

where the switching functions $n_u(t)$ and $n_l(t)$ are determined by the controller employed in the MMC, which can be expressed as

$$\begin{cases} n_u(t) = \frac{1}{2}\left[1 - m\cos(\omega_1 t + \theta_{m1}) - m_2 \cos(2\omega_1 t + \theta_{m2}) \right. \\ \qquad \left. + \sum_{n=3}^{\infty} m_n \cos(n\omega t + \theta_n)\right] \\ n_l(t) = \frac{1}{2}\left[1 + m\cos(\omega_1 t + \theta_{m1}) - m_2 \cos(2\omega_1 t + \theta_{m2}) \right. \\ \qquad \left. + \sum_{n=3}^{\infty} m_n \cos(n\omega t + \theta_n)\right] \end{cases} \tag{20}$$

where m and θ_{m1} are the modulation index and phase of the fundamental modulation voltage generated by the fundamental controller, m_2 and θ_{m2} are the modulation index and phase of the second harmonic modulation voltage generated by the second harmonic circulating current controller. Additionally, the harmonic components above second-order in (20) are normally zero, i.e., $m_n = 0 (n \geq 3)$.

It is noted that there are significant steady-state harmonic components in the state variables such as $i_c(t)$, $v_{cu}^{\sum}(t)$, and $v_{cl}^{\sum}(t)$, which are caused by the operation characteristics of the MMC [4]. For instance, the circulating current $i_c(t)$ contains dc and second harmonic components as well as other even harmonics, which are negligibly small in normal operation. Moreover, the capacitor voltages $v_{cu}^{\sum}(t)$ and $v_{cl}^{\sum}(t)$ theoretically contain all the harmonics. Therefore, in order to accurately represent the multiharmonic MMC model, the HSS modeling method, in which harmonics of state variables, inputs, and outputs are posed separately in a state-space form, is introduced to model the MMC in this work.

Following the HSS modeling procedure introduced in (1)–(9), the time-domain state-space model of the MMC that is formulated as (3) and (16)–(20) can be converted into the HSS model that is expressed in (4), where the elements X_h, U_h, A_h, and B_h are shown in (21)–(24). It is noted that each element of the Toeplitz matrix $\mathbf{A}$ is also a matrix that has the same size as $A(t)$, whose element can be calculated by applying (2) to the corresponding element of $A(t)$

$$X_{\pm h} = \left[I_{c\pm h}, V_{cu\pm h}^{\sum}, V_{cl\pm h}^{\sum}, I_{g\pm h} \right] \tag{21}$$

$$U_0 = [V_{\rm dc}], U_{\pm h} = [0] \quad (h \geq 1) \tag{22}$$

$$A_0 = \begin{bmatrix} -\frac{R}{L} & -\frac{1}{4L} & -\frac{1}{4L} & 0 \\ \frac{1}{2C_{\rm arm}} & 0 & 0 & \frac{1}{4C_{\rm arm}} \\ \frac{1}{2C_{\rm arm}} & 0 & 0 & -\frac{1}{4C_{\rm arm}} \\ 0 & -\frac{1}{2L} & \frac{1}{2L} & -\frac{R+2Z_L}{L} \end{bmatrix} \tag{23a}$$

$$A_{\pm 1} = \begin{bmatrix} 0 & \frac{m e^{\pm j\theta_{m1}}}{8L} & -\frac{m e^{\pm j\theta_{m1}}}{8L} & 0 \\ -\frac{m e^{\pm j\theta_{m1}}}{4C_{\rm arm}} & 0 & 0 & -\frac{m e^{\pm j\theta_{m1}}}{8C_{\rm arm}} \\ \frac{m e^{\pm j\theta_{m1}}}{4C_{\rm arm}} & 0 & 0 & -\frac{m e^{\pm j\theta_{m1}}}{8C_{\rm arm}} \\ 0 & \frac{m e^{\pm j\theta_{m1}}}{4L} & \frac{m e^{\pm j\theta_{m1}}}{4L} & 0 \end{bmatrix} \tag{23b}$$

$$A_{\pm 2} = \begin{bmatrix} 0 & \frac{m_2 e^{\pm j\theta_{m2}}}{8L} & \frac{m_2 e^{\pm j\theta_{m2}}}{8L} & 0 \\ -\frac{m_2 e^{\pm j\theta_{m2}}}{4C_{\rm arm}} & 0 & 0 & -\frac{m_2 e^{\pm j\theta_{m2}}}{8C_{\rm arm}} \\ -\frac{m_2 e^{\pm j\theta_{m2}}}{4C_{\rm arm}} & 0 & 0 & \frac{m_2 e^{\pm j\theta_{m2}}}{8C_{\rm arm}} \\ 0 & \frac{m_2 e^{\pm j\theta_{m2}}}{4L} & -\frac{m_2 e^{\pm j\theta_{m2}}}{4L} & 0 \end{bmatrix} \tag{23c}$$

$$A_{\pm h} = \begin{bmatrix} 0 & 0 & 0 & 0 \\ 0 & 0 & 0 & 0 \\ 0 & 0 & 0 & 0 \\ 0 & 0 & 0 & 0 \end{bmatrix} \quad (h \geq 3) \tag{23d}$$

$$B_0 = \left[\frac{1}{2L}, 0, 0, 0 \right]^T, \quad B_{\pm h} = [0, 0, 0, 0]^T \quad (h \geq 1). \tag{24}$$

TABLE I
MAIN ELECTRICAL PARAMETERS OF THE MMC

Parameter	Value
Rated power	50 MW
Rated frequency	50 Hz
Rated dc voltage	320 kV
Rated ac voltage	166 kV
Submodule number per arm	20
Submodule capacitor	140 μF
Arm inductance	360 mH
Arm resistance	1 Ω

Letting the left side of (4) to be zero, the steady-state harmonics of state variables can, thus, be calculated by

$$\mathbf{X}_{ss} = -(\mathbf{A} - \mathbf{Q})^{-1}(\mathbf{BU}). \tag{25}$$

In order to validate the precision of the HSS model developed in this paper, a comparison between the results from the HSS model and the nonlinear time-domain simulation model has been carried out, where the nonlinear time-domain simulation model is implemented in MATLAB/Simulink, and the HSS model is performed by using an m-file in MATLAB. In this case, open-loop control is adopted by directly setting the fundamental-frequency reference voltage. The harmonic order considered in the HSS model of the MMC is $h = 3$, and the main electrical parameters of the MMC in the simulation are listed in Table I. As shown in Fig. 3, it can be seen that the results between the HSS model and the time-domain simulation model have a good match, which indicates that the HSS model of the MMC developed in this paper is able to capture all the steady-state harmonics in the circulating current and capacitor voltage, and is accurate enough for harmonic steady-state studies. It is noted that the results from the HSS model can be converted into the time-domain signals by using (1).

C. HSS-Based Small-Signal Model of the MMC

In Section II-B, the HSS-based large-signal model of the MMC is first developed, which aims at showing the high accuracy of the proposed HSS model and also providing the steady-state solution for the subsequent small-signal modeling. Since the steady-state operation point of the MMC is periodically time-varying rather than constant, the harmonic linearization principle needs to be applied in order to derive the small-signal model of the MMC.

By applying small perturbation analysis to the state-space equation of the MMC formulated in (3) and (16)–(19), the small-signal state-space equation of the MMC can be obtained as

$$\dot{x}_p(t) = A_p(t)x_p(t) + B_p(t)u_p(t) \tag{26}$$

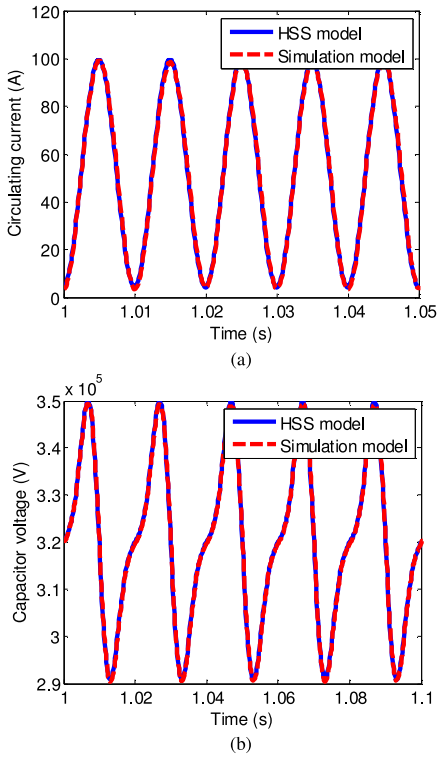

Fig. 3. Validation for the HSS model of the MMC. (a) Circulating current i_c. (b) Capacitor voltage $\sum_{v_{cu}}$.

where

$$x_p(t) = \left[i_{cp}(t), v_{cup}^{\sum}(t), v_{clp}^{\sum}(t), i_{gp}(t)\right]^T \tag{27}$$

$$u_p(t) = [n_{up}(t), n_{lp}(t), v_p(t)]^T \tag{28}$$

$$A_p(t) = \begin{bmatrix} -\dfrac{R}{L} & -\dfrac{n_{us}(t)}{2L} & -\dfrac{n_{ls}(t)}{2L} & 0 \\ \dfrac{n_{us}(t)}{C_{\text{arm}}} & 0 & 0 & \dfrac{n_{us}(t)}{2C_{\text{arm}}} \\ \dfrac{n_{ls}(t)}{C_{\text{arm}}} & 0 & 0 & -\dfrac{n_{ls}(t)}{2C_{\text{arm}}} \\ 0 & -\dfrac{n_{us}(t)}{L} & \dfrac{n_{ls}(t)}{L} & -\dfrac{R+2Z_L}{L} \end{bmatrix} \tag{29}$$

$$B_p(t) = \begin{bmatrix} -\dfrac{v_{cus}^{\sum}(t)}{2L} & -\dfrac{v_{cls}^{\sum}(t)}{2L} & 0 \\ \dfrac{1}{C_{\text{arm}}}\left(i_{cs}(t) + \dfrac{i_{gs}(t)}{2}\right) & 0 & 0 \\ 0 & \dfrac{1}{C_{\text{arm}}}\left(i_{cs}(t) - \dfrac{i_{gs}(t)}{2}\right) & 0 \\ -\dfrac{v_{cus}^{\sum}(t)}{L} & \dfrac{v_{cls}^{\sum}(t)}{L} & -\dfrac{2}{L} \end{bmatrix} \tag{30}$$

in which the subscripts "s" and "p" denote steady-state and perturbation components, respectively. The small perturbations $n_{up}(t)$ and $n_{lp}(t)$ of the switching functions depend on the controller dynamics, which will be discussed in the next section.

According to the operation principle of the MMC, the injected small perturbation voltage will lead to perturbations in all variables at frequencies that are listed in (31). Since these frequency components may have important effects on the MMC impedance response, all these frequency components will be included in the impedance modeling in this paper

$$\omega_p, \omega_p \pm \omega_1, \omega_p \pm 2\omega_1, \ldots, \omega_p \pm h\omega_1. \tag{31}$$

Accordingly, the small-signal HSS model of the MMC can be obtained as follows by using the HSS modeling procedure to the time-domain small-signal state-space equation of the MMC that is formulated in (26)

$$s\mathbf{X}_p = (\mathbf{A}_p - \mathbf{Q}_p)\mathbf{X}_p + \mathbf{B}_p\mathbf{U}_p \tag{32}$$

where $\mathbf{X_p}$, $\mathbf{U_p}$, and $\mathbf{Q}_p$ are given in (33)–(35), respectively, in which the subscript "$p \pm h$" denotes the perturbation component at frequency "$\omega_p \pm h\omega_1$." It is noted that the diagonal matrix $\mathbf{Q}_p$ contains all the perturbation frequencies that are defined in (31), which means that this model considers all the frequency coupling effects. Additionally, the Toeplitz matrices $\mathbf{A}_p$ and $\mathbf{B}_p$ depend on the specific control scheme used in the MMC, which is given in Section III

$$\begin{aligned}
\mathbf{X}_p &= [X_{p-h}, \ldots, X_p, \ldots, X_{p+h}]^T \\
X_{p\pm h} &= \left[I_{cp\pm h}, V^{\Sigma}_{\mathrm{cup}\pm h}, V^{\Sigma}_{clp\pm h}, I_{gp\pm h}\right] \qquad (33)\\
\mathbf{U}_p &= [U_{p-h}, \ldots, U_p, \ldots, U_{p+h}]^T \\
U_p &= [V_p], U_{p\pm h} = [0](h \geq 1) \qquad (34)\\
\mathbf{Q}_p &= diag[j(\omega_p - h\omega_1)\cdot I, \ldots, j\omega_p \cdot I, \ldots, j \\
&\quad \times (\omega_p + h\omega_1)\cdot I]. \qquad (35)
\end{aligned}$$

III. HSS-Based Small-Signal Impedance Modeling of the MMC

A. Definition of the Small-Signal Impedance of the MMC

According to the harmonic linearization principle, by injecting a small sinusoidal perturbation voltage at frequency ω_p in the ac side of the MMC and then calculating the corresponding ac-side current response at the perturbation frequency ω_p, the ac-side small-signal impedance of the MMC can, thus, be obtained by calculating the ratio of the resulting complex voltage to current at the perturbation frequency ω_p, which is defined as

$$Z_{\mathrm{MMC}}(j\omega_p) = -\frac{\boldsymbol{V}_{gp}}{\boldsymbol{I}_{gp}} \tag{36}$$

where the bold letters $\boldsymbol{V}_{gp}$ and $\boldsymbol{I}_{gp}$ are the complex phasors of the resulting perturbation voltage and current at frequency ω_p. Additionally, the perturbation voltage $\boldsymbol{V}_{gp}$ can be expressed as

$$\boldsymbol{V}_{gp} = \boldsymbol{V}_p + Z_L\boldsymbol{I}_{gp} \tag{37}$$

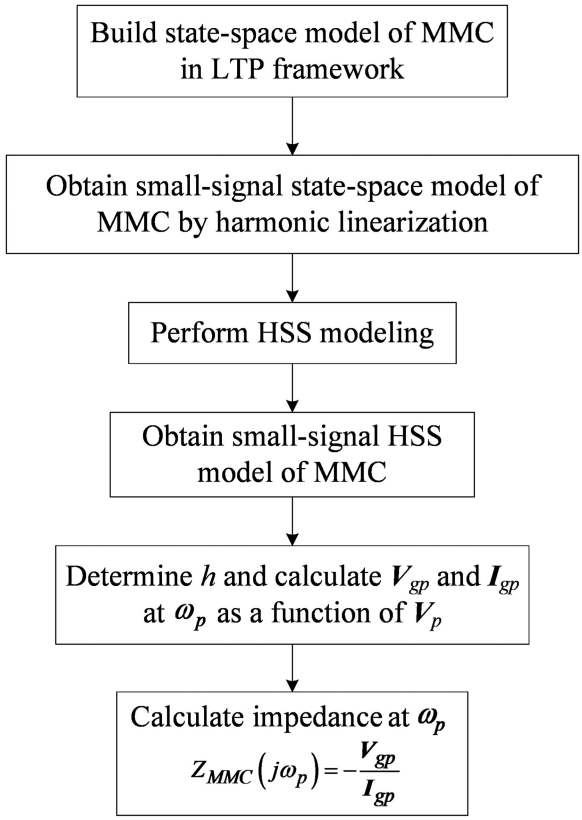

Fig. 4. Flowchart of the small-signal impedance modeling of the MMC based on HSS modeling.

in which the perturbation input voltage $\boldsymbol{V}_p$ is predefined, and the resulting perturbation current $\boldsymbol{I}_{gp}$ can be solved as a function of the perturbation input voltage $\boldsymbol{V}_p$ based on the small-signal HSS model of the MMC.

Fig. 4 shows the flowchart of the small-signal impedance modeling of the MMC based on the HSS modeling method.

In order to uncover the impact of the control strategies and internal dynamics of the MMC on the small-signal impedance, three cases are considered in the impedance modeling in this paper, i.e., open-loop control, ac voltage closed-loop control, and circulating current closed-loop control.

B. Impedance Modeling of the MMC With Open-Loop Control

If open-loop control is used, the fundamental modulation voltage is given directly and the second harmonic component in (20) is zero. As a result, the switching functions n_u and n_l are not perturbed by the injected small perturbation voltage, which means $n_{up} = n_{lp} = 0$. Hence, $u_p(t)$ and $B_p(t)$ of the small-signal state-space equation of the MMC in (26) become the following equations, respectively, while $x_p(t)$ and $A_p(t)$ remain the same as (27) and (29)

$$u_{p\_op}(t) = [v_p(t)] \tag{38}$$

$$B_{p\_op}(t) = \left[0, 0, 0, -\frac{2}{L}\right]^T. \tag{39}$$

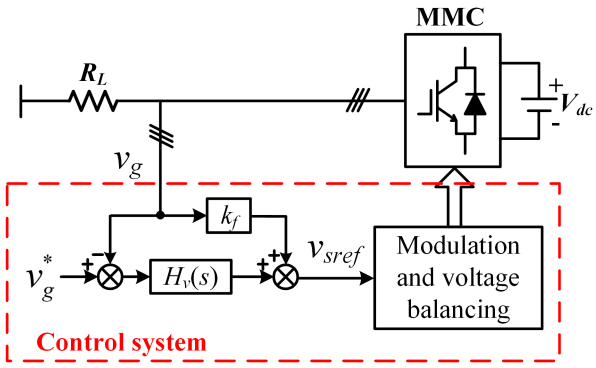

Fig. 5. Diagram of the ac voltage closed-loop control.

Accordingly, the small-signal HSS model of the MMC with open-loop control can be obtained as (32), where the elements of the Toeplitz matrix $\mathbf{A}_p$ are identical to (23), whereas the elements $A_{\pm 2}$ are zero matrices in this case. Additionally, the elements of the Toeplitz matrix $\mathbf{B}_p$ are shown

$$B_0 = \left[0, 0, 0, -\frac{2}{L}\right]^T, \quad B_{\pm h} = [0, 0, 0, 0]^T (h \geq 1). \tag{40}$$

Ignoring the transient behavior of the perturbation signals, that is, letting the left-hand side of (32) to be zero, the small perturbation components of the state variables at each perturbation frequency in (31) can be solved by

$$\mathbf{X}_p = -(\mathbf{A}_p - \mathbf{Q}_p)^{-1}(\mathbf{B}_p \mathbf{U}_p). \tag{41}$$

It should be pointed out that the harmonic order h must be predetermined in order to solve (41), and all the small perturbation components of the state variables can be calculated as a function of the injected perturbation voltage $\boldsymbol{V}_p$, where $\boldsymbol{V}_p$ is also predefined. According to the definition of the small-signal impedance in (36), only the resulting perturbation voltage and current at frequency ω_p in the ac side of the MMC need to be concerned. From (41), the resulting perturbation current $\boldsymbol{I}_{gp}$ at frequency ω_p can be calculated as a function of the perturbation input voltage $\boldsymbol{V}_p$. Subsequently, the resulting perturbation voltage $\boldsymbol{V}_{gp}$ at frequency ω_p can be figured out by substituting $\boldsymbol{I}_{gp}$ into (37). Finally, the ac-side small-signal impedance of the MMC at frequency ω_p can be calculated by substituting $\boldsymbol{V}_{gp}$ and $\boldsymbol{I}_{gp}$ into (36). It is worth noting that the higher the harmonic order h, the more accurate the MMC impedance model. Nevertheless, the analytical impedance expression of the MMC with high harmonic order will become much more complex and lengthy. However, in general, the MMC impedance model is accurate enough if the harmonic order $h \geq 3$, which will be further confirmed in the following section.

C. Impedance Modeling of the MMC With AC Voltage Closed-Loop Control

Fig. 5 depicts the diagram of the ac voltage closed-loop control in a three-phase stationary frame, where $H_v(s)$ is a proportional-resonant (PR) controller to achieve zero steady-state errors for sinusoidal quantities, and k_f is the feedforward gain to improve dynamic response.

The transfer function of the ac voltage regulator $H_v(s)$ is

$$H_v(s) = K_p + \frac{K_r s}{s^2 + \omega_1^2} \tag{42}$$

where K_p and K_r are the proportional and resonant gains of the PR controller, respectively.

The reference modulation voltage can be obtained as follows, where the subscript "x" $(x = a, b, c)$ is omitted for simplicity:

$$v_{\text{sref}}(s) = \{H_v(s)[v_g^*(s) - v_g(s)] + k_f v_g(s)\} G_d(s) \tag{43}$$

where $G_d(s)$ represents the digital control delay of 1.5 sampling periods.

Applying linearization to (43), one can obtain

$$v_{\text{sref}p}(s) = [k_f - H_v(s)] G_d(s) v_{gp}(s). \tag{44}$$

Hence, the small perturbations n_{up} and n_{lp} of the switching functions can be obtained as

$$\begin{cases} \boldsymbol{n}_{up} = -\dfrac{(k_f - H_v)G_d}{V_{dc}} \boldsymbol{v}_{gp} \triangleq -G_v \boldsymbol{v}_{gp} \\ \boldsymbol{n}_{lp} = \dfrac{(k_f - H_v)G_d}{V_{dc}} \boldsymbol{v}_{gp} \triangleq G_v \boldsymbol{v}_{gp} \end{cases} \tag{45}$$

where the bold letters represent the complex phasors at the perturbation frequency.

Combining (45), (37), and (26)–(30), and applying the HSS modeling procedure that is introduced in (1)–(9), the small-signal HSS model of the MMC with ac voltage closed-loop control can be obtained like (32), where $\mathbf{X}_p, \mathbf{U}_p$, and $\mathbf{Q}_p$ are the same as (33)–(35), and the elements of $\mathbf{A}_p$ and $\mathbf{B}_p$ are given in (46), (46b) shown at the bottom the next page and (47), respectively, in which the subscript "h" $(h = 0, 1, 2 \ldots)$ of the state variables represents the Fourier coefficient of the hth harmonic of the state variable under steady state, which can be calculated by (25)

$$A_0 = \begin{bmatrix} -\frac{R}{L} & -\frac{1}{4L} & -\frac{1}{4L} & \frac{G_v\left(V_{cu0}^{\Sigma} - V_{cl0}^{\Sigma}\right)}{2L} Z_L \\ \frac{1}{2C_{\text{arm}}} & 0 & 0 & \frac{1}{4C_{\text{arm}}} - \frac{G_v\left(I_{c0} + \frac{I_{g0}}{2}\right)}{C_{\text{arm}}} Z_L \\ \frac{1}{2C_{\text{arm}}} & 0 & 0 & -\frac{1}{4C_{\text{arm}}} + \frac{G_v\left(I_{c0} - \frac{I_{g0}}{2}\right)}{C_{\text{arm}}} Z_L \\ 0 & -\frac{1}{2L} & \frac{1}{2L} & -\frac{R}{L} + \frac{G_v\left(V_{cu0}^{\Sigma} + V_{cl0}^{\Sigma}\right) - 2}{L} Z_L \end{bmatrix} \tag{46a}$$

$$A_{\pm h}=\begin{bmatrix} 0 & 0 & 0 & \dfrac{G_v\left(V_{cu\pm h}^{\Sigma}-V_{cl\pm h}^{\Sigma}\right)}{2L}Z_L \\ 0 & 0 & 0 & -\dfrac{G_v\left(I_{c\pm h}+\dfrac{I_{g\pm h}}{2}\right)}{C_{\rm arm}}Z_L \\ 0 & 0 & 0 & \dfrac{G_v\left(I_{c\pm h}-\dfrac{I_{g\pm h}}{2}\right)}{C_{\rm arm}}Z_L \\ 0 & 0 & 0 & \dfrac{G_v\left(V_{cu\pm h}^{\Sigma}+V_{cl\pm h}^{\Sigma}\right)}{L}Z_L \end{bmatrix} \quad (h\geq 2) \tag{46c}$$

$$B_0=\left[\frac{G_v\left(V_{cu0}^{\Sigma}-V_{cl0}^{\Sigma}\right)}{2L},-\frac{G_v\left(I_{c0}+\frac{I_{g0}}{2}\right)}{C_{\rm arm}},\frac{G_v\left(I_{c0}-\frac{I_{g0}}{2}\right)}{C_{\rm arm}},\frac{G_v\left(V_{cu0}^{\Sigma}+V_{cl0}^{\Sigma}\right)-2}{L}\right]^T \tag{47a}$$

$$B_{\pm h}=\left[\frac{G_v\left(V_{cu\pm h}^{\Sigma}-V_{cl\pm h}^{\Sigma}\right)}{2L},-\frac{G_v\left(I_{c\pm h}+\frac{I_{g\pm h}}{2}\right)}{C_{\rm arm}},\frac{G_v\left(I_{c\pm h}-\frac{I_{g\pm h}}{2}\right)}{C_{\rm arm}},\frac{G_v\left(V_{cu\pm h}^{\Sigma}+V_{cl\pm h}^{\Sigma}\right)}{L}\right]^T (h\geq 1)\,. \tag{47b}$$

In the same way, by substituting (34), (35), (46) and (47) into (41), the resulting perturbation current $\boldsymbol{I}_{gp}$ at frequency ω_p can be solved by (41), and then the resulting perturbation voltage $\boldsymbol{V}_{gp}$ at frequency ω_p can be obtained by (37). Hence, the ac-side small-signal impedance of the MMC with ac voltage closed-loop control can then be calculated by (36).

D. Impedance Modeling of the MMC With Circulating Current Closed-Loop Control

The circulating current control strategies commonly used in the MMC can be categorized into two groups, one is based on PI controllers in the dq rotating frame, the other is based on PR controllers in the abc stationary frame. However, both of these two strategies are able to effectively suppress the harmonic circulating currents. It is worth noting that no matter the integral part of the PI controller or the resonant part of the PR controller, it can mainly affect the voltage and current signals at around the designated frequency while having little impact on those signals at other frequencies. In other words, the impedance–frequency characteristics of the MMC are mainly influenced by the proportional part of the controller. Therefore, to reveal the influence mechanism of the circulating current closed-loop control on the impedance–frequency characteristics of the MMC, a proportional controller based circulating current control [3] is used in this paper, as presented in Fig. 6, where the modified modulation voltage $v_{\rm cref}$ is added to the original fundamental modulation voltage. The circulating current reference is $i_{cx}^{*}=P/3/V_{\rm dc}$, where P is the active power.

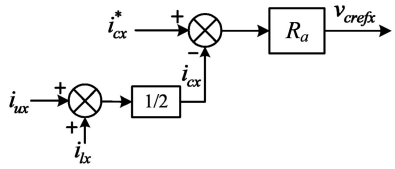

Fig. 6. Diagram of the circulating current closed-loop control.

In a similar way to that with the ac voltage closed-loop control, we can derive the ac-side small-signal impedance of the MMC with circulating current closed-loop control. Due to the limited space, the detailed derivation process is no longer given in this paper.

IV. Application of the HSS-Based Small-Signal Impedance Model: Stability Analysis of the MMC-HVDC-Connected Wind Farm

Fig. 7 shows the structure diagram of wind farm integration through an MMC-HVDC transmission system, where the wind farm consists of full-power wind turbines based on two-level VSCs, and the MMC-HVDC transmission system comprises a wind farm side MMC station (WFMMC), a grid-side MMC station (GSMMC), and dc transmission lines. The MMC topology for both WFMMC and GSMMC is shown in Fig. 1.

$$A_{\pm 1}=\begin{bmatrix} 0 & \dfrac{me^{\pm j\theta_{m1}}}{8L} & -\dfrac{me^{\pm j\theta_{m1}}}{8L} & \dfrac{G_v(V_{cu\pm 1}^{\Sigma}-V_{cl\pm 1}^{\Sigma})}{2L}Z_L \\ -\dfrac{me^{\pm j\theta_{m1}}}{4C_{\rm arm}} & 0 & 0 & -\dfrac{me^{\pm j\theta_{m1}}}{8C_{\rm arm}}-\dfrac{G_v\left(I_{c\pm 1}+\dfrac{I_{g\pm 1}}{2}\right)}{C_{\rm arm}}Z_L \\ \dfrac{me^{\pm j\theta_{m1}}}{4C_{\rm arm}} & 0 & 0 & -\dfrac{me^{\pm j\theta_{m1}}}{8C_{\rm arm}}+\dfrac{G_v\left(I_{c\pm 1}-\dfrac{I_{g\pm 1}}{2}\right)}{C_{\rm arm}}Z_L \\ 0 & \dfrac{me^{\pm j\theta_{m1}}}{4L} & \dfrac{me^{\pm j\theta_{m1}}}{4L} & \dfrac{G_v\left(V_{cu\pm 1}^{\Sigma}+V_{cl\pm 1}^{\Sigma}\right)}{L}Z_L \end{bmatrix} \tag{46b}$$

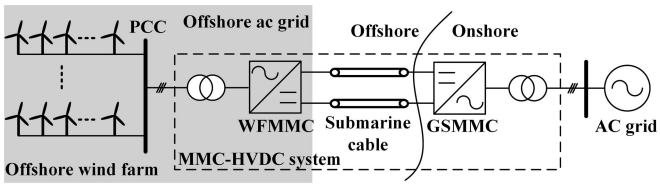

Fig. 7. Structure diagram of wind farm integration via an MMC-HVDC transmission system.

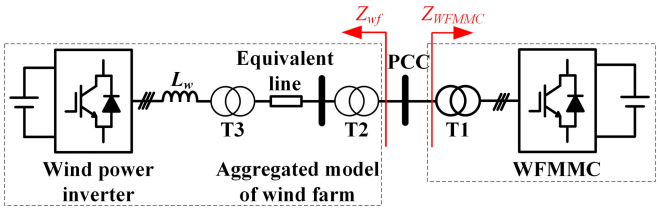

Fig. 8. Simplified circuit structure of the interconnected system.

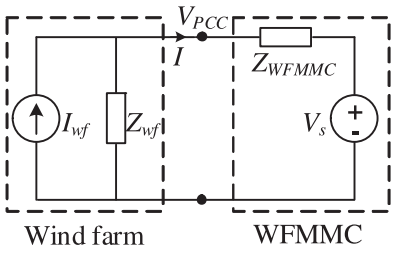

Fig. 9. Small-signal impedance representation of the interconnected system.

For simplicity, the simplified circuit structure diagram of the interconnected system is presented in Fig. 8, which can be obtained by applying the following procedures.

1) The wind farm is aggregated into one wind turbine generator.
2) The generator side dynamics (including turbine mechanical and generator side converter) are ignored, since the grid side converter of the wind turbine generator is decoupled with the generator side by the dc-link capacitor.
3) It is assumed that the ac power grid is strong and the control bandwidth of the dc voltage loop of the GSMMC is less than the subsynchronous oscillation (SSO) frequency under study; thus, the GSMMC can be simply replaced with a dc voltage source.

The small-signal impedance representation of the interconnected system is shown in Fig. 9. The wind farm is modeled by its Norton equivalent circuit consisting of a current source $I_{\rm wf}$ in parallel with the wind farm impedance $Z_{\rm wf}$. The WFMMC is modeled by its Thevenin equivalent circuit in the form of an ideal voltage source V_s in series with the WFMMC impedance $Z_{\rm WFMMC}$. Hence, the voltage stability at the point of common coupling (PCC) of the interconnected system is determined by the impedance ratio $Z_{\rm WFMMC}/Z_{\rm wf}$, i.e., the voltage at the PCC is stable if and only if $Z_{\rm WFMMC}/Z_{\rm wf}$ satisfies the Nyquist stability criterion. In addition, the wind farm impedance $Z_{\rm wf}$ includes the wind power inverter impedance, step-up transformer impedances, and collection line impedance, and the WFMMC impedance $Z_{\rm WFMMC}$ can be obtained by adding the converter transformer impedance and the MMC impedance, which needs to be converted to the PCC side of the converter transformer.

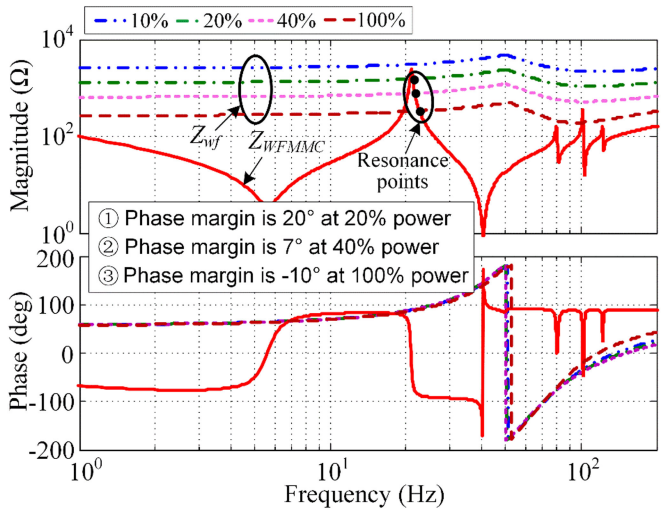

Fig. 10. AC-side impedance–frequency characteristics of the WFMMC and wind farm under different power conditions.

Fig. 10 shows the ac-side impedance–frequency characteristics of the WFMMC and wind farm under different power level conditions, i.e., 10%, 20%, 40%, and 100% of the rated power, where the ac voltage closed-loop control is used in the WFMMC without circulating current control and the wind turbine operates at unity power factor. It can be seen that the magnitude of the wind farm impedance decreases as the output active power of the wind farm increases, while the phase of the wind farm impedance is almost unchanged. It is worth noting that the magnitude-frequency characteristics of the WFMMC impedance and wind farm impedance can intersect around the low-frequency resonance peak of the WFMMC impedance magnitude, where the corresponding phase margin (PM) of the interconnected system becomes smaller as the wind farm output power becomes larger. That is the key reason why the SSO phenomenon can happen in an MMC-HVDC system for wind farm integration. However, it should be pointed out that the intersection does not always arise, which depends on many factors such as the wind farm output power, control strategies, controller parameters of both the WFMMC and wind farm, etc.

Fig. 11 shows the simulated results of the interconnected system under 20% of the rated power condition. It is seen that the interconnected system is stable, but with slight oscillations, due to the small PM (about 20° as predicted in Fig. 10). Furthermore, the fast Fourier transform analysis shows that the dominant oscillation frequency is around 22 Hz, which is consistent with the theoretical analysis in Fig. 10. Fig. 12 shows the simulated results of the interconnected system at the rated power. As can be seen, the ac voltages and currents are seriously distorted, which indicates that the interconnected system becomes unstable. It should be pointed out that the reason why the unstable case presents the sustained equal amplitude oscillation rather than the divergent oscillation is because of the effect of the voltage-limiting in the current controller of the wind power inverter.

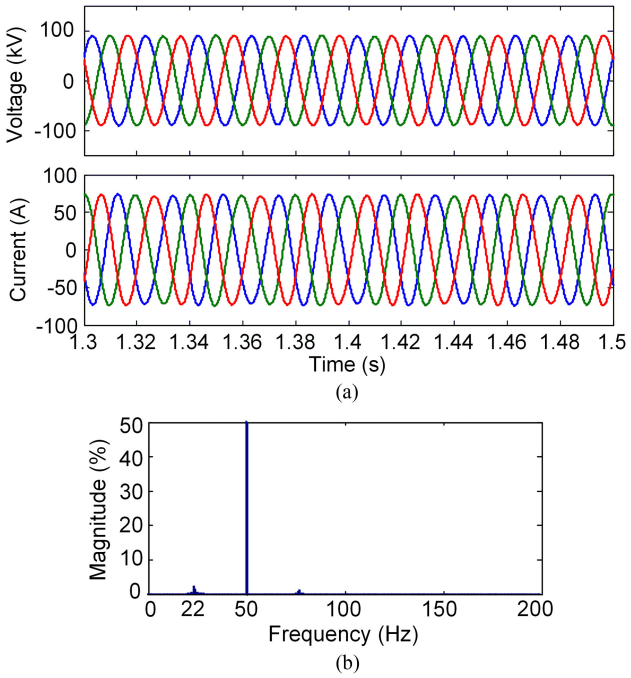

Fig. 11. Simulated results of the interconnected system under 20% of the rated power condition. (a) Three-phase ac phase voltages and currents at the PCC of the interconnected system. (b) Frequency analysis of the ac phase voltage.

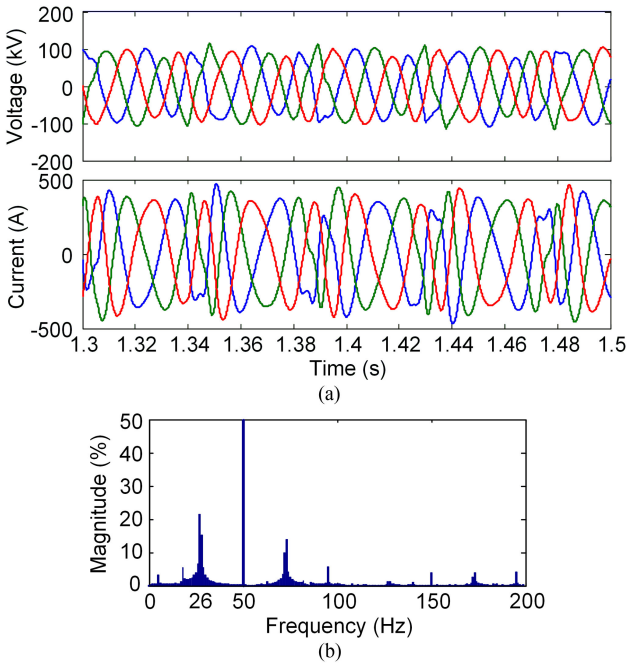

Fig. 12. Simulated results of the interconnected system under the rated power condition. (a) Three-phase ac phase voltages and currents at the PCC of the interconnected system. (b) Frequency analysis of the ac phase voltage.

V. Simulation and Experimental Verification

A. Simulation Verification

To verify the derived impedance models of the MMC, a nonlinear time-domain simulation model of a three-phase MMC with a three-phase resistance load has been built by using MATLAB/Simulink. In the simulation, the ac-side small-signal impedance of the MMC is measured by means of injecting a series of small perturbation voltage signals at different frequencies in the ac side of the MMC. Then by measuring the resulting perturbation current signals, the ac-side small-signal impedance can be readily calculated for each frequency. The main electrical parameters of the MMC in the simulation are the same as those in Table I.

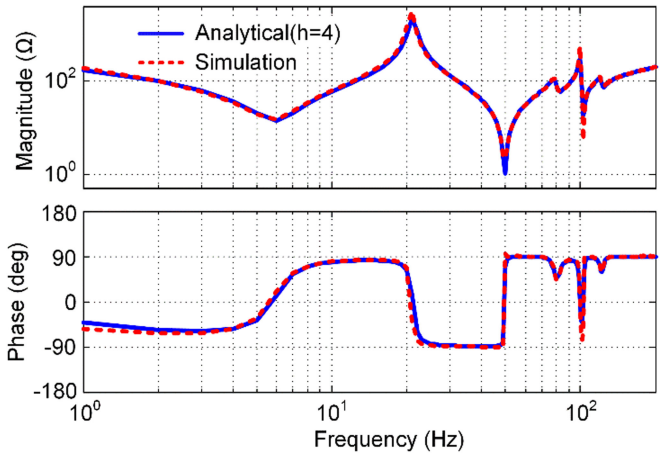

Fig. 13. Analytical and simulation measured impedances of the MMC with open-loop control.

Fig. 13 shows the comparison between the analytical and simulation measured ac-side small-signal impedances of the MMC with open-loop control, where the harmonic order h of the analytical model is selected as 4. It is seen that the analytical impedance matches well with the measured result in the simulation, which validates the analytical impedance model. Furthermore, it can be seen that there are several resonance points in the ac-side impedance of the MMC below 150 Hz, where the resonance concave at the fundamental frequency is generated by the fundamental voltage control, and the other resonances are originated from the internal dynamics of the MMC. And, more remarkable, the resonance peak around 21 Hz caused by the internal circulating current resonance of the MMC is likely to result in oscillations by interacting with the impedance of the load converter. The frequency at the resonance peak mainly depends on the main circuit parameters of the MMC, such as the arm inductance, SM capacitance, SM number per arm, etc.

Fig. 14 shows the impact of the harmonic order considered in the HSS model of the MMC on the accuracy of the analytical MMC impedance model. It can be observed that the harmonic order considered in the HSS model of the MMC has a great impact on the accuracy of the analytical impedance model. The higher the harmonic order considered in the HSS model, the more accurate the analytical impedance model. However, only several significant low-order harmonics play dominant roles in the MMC impedance response. Generally, it can be concluded that the analytical MMC impedance model is accurate enough if the harmonic order $h \geq 3$. In addition, it is worth noting that if the MMC internal harmonic dynamics are not considered in the impedance modeling, i.e., $h = 0$, the resulting impedance model cannot reflect the low-frequency resonance characteristics of the

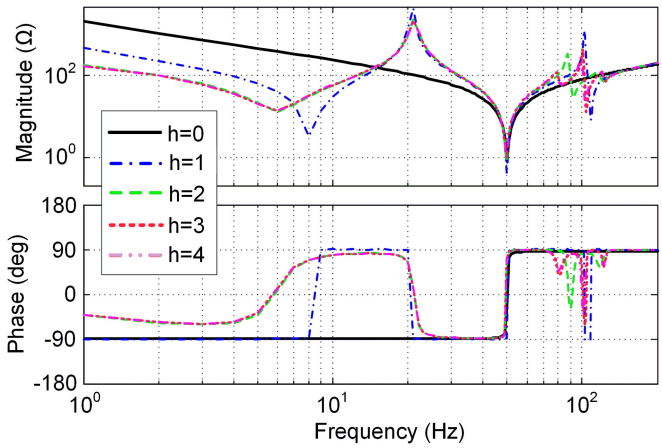

Fig. 14. Impact of the harmonic order considered in the HSS model on the accuracy of the analytical MMC impedance model with open-loop control.

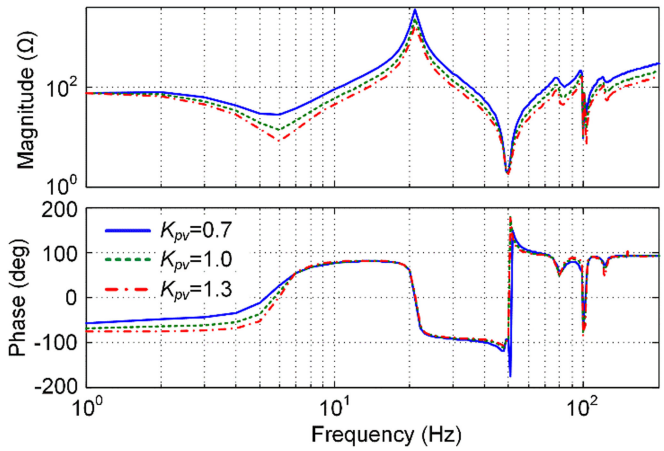

Fig. 16. Impact of the proportional gain of the ac voltage controller on the MMC impedance.

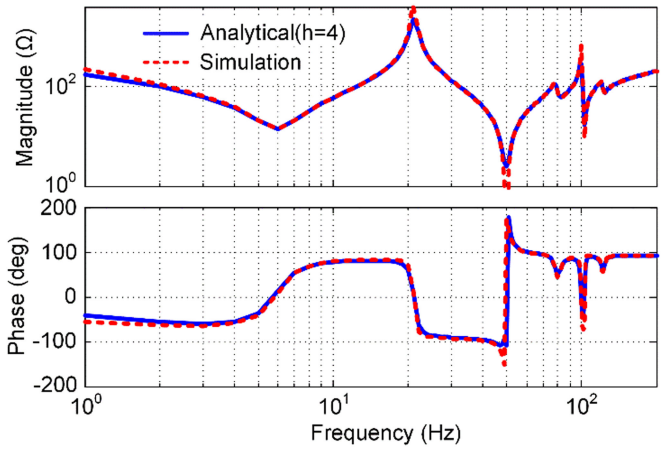

Fig. 15. Analytical and simulation measured impedances of the MMC with ac voltage closed-loop control.

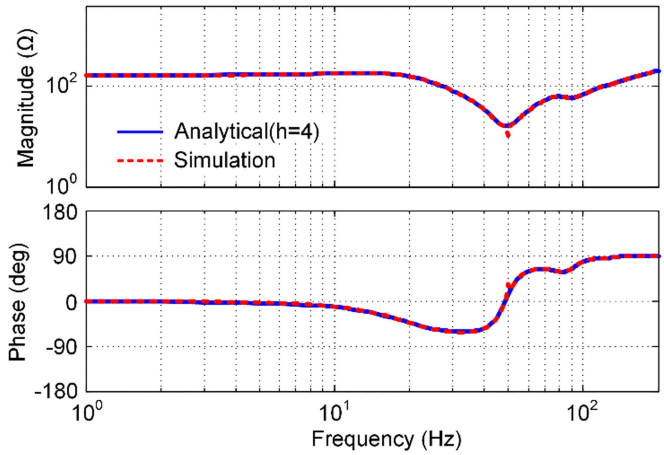

Fig. 17. Analytical and simulation measured impedances of the MMC with circulating current closed-loop control.

MMC. Therefore, it is essential to consider the MMC internal harmonic dynamics in the MMC impedance modeling in order to accurately capture the low-frequency resonance characteristics of the MMC.

Fig. 15 presents the comparison between the analytical and simulation measured ac-side small-signal impedances of the MMC with ac voltage closed-loop control (where $K_{pv} = 1, K_{rv} = 20$), which verifies the analytical MMC impedance model as well. Furthermore, by comparing Figs. 15 and 13, it can be observed that the shape of the ac-side small-signal impedance with ac voltage closed-loop control is very similar to that with open-loop control, where the major difference is at the fundamental frequency (50 Hz hereof) because of the resonant part of the ac voltage controller. Besides, it can be seen from Fig. 16 how the proportional gain of the ac voltage controller affects the ac-side impedance of the MMC, where the larger the proportional gain of the ac voltage controller, the smaller the magnitude of the MMC impedance in the entire frequency range, but having little impact on the resonance frequencies. In addition, it needs to be pointed out that the resonant gain of the ac voltage controller has less effect on the MMC impedance except at the fundamental frequency.

Fig. 17 shows the comparison between the analytical and simulation measured ac-side small-signal impedances of the MMC with circulating current closed-loop control (where $R_a = 20$). As can be seen, the analytical impedance has a good agreement with the measured result in the simulation, which validates the analytical MMC impedance model. Moreover, it is worth noting that the low-frequency resonance characteristics of the MMC are well suppressed by the circulating current controller, which indicates that the circulating current controller can provide internal damping to the MMC system. In other words, the proportional gain R_a of the circulating current controller essentially plays a role of a virtual arm resistance. Moreover, the impedance responses with different harmonic orders considered in the HSS model of the MMC with the circulating current closed-loop control are shown in Fig. 18, where it can be seen that the harmonic order considered in the HSS model has similar impact characteristics on the impedance responses under the circulating current closed-loop control compared to Fig. 14. Nevertheless, the differences among the

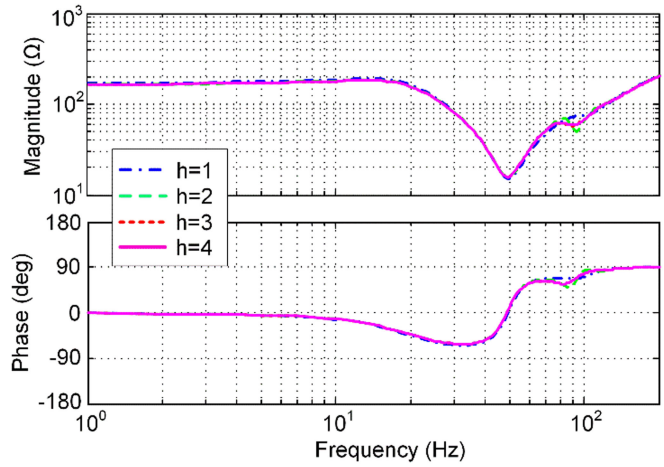

Fig. 18. Impact of the harmonic order h considered in the HSS model on the accuracy of the analytical MMC impedance model with circulating current closed-loop control.

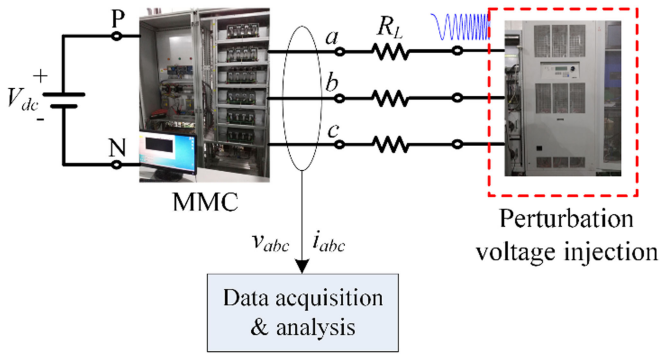

Fig. 19. Schematic diagram of the experimental setup.

impedance responses with different harmonic orders under the circulating current closed-loop control are much smaller due to the damping effect of the circulating current controller.

B. Experimental Verification

To further validate the proposed MMC impedance models, the small-signal impedance measurements on a three-phase scale-down MMC experimental setup have also been carried out. The topology of the MMC experimental setup is identical to that in Fig. 1. The California Instruments MODEL RS90 programmable power source is used as the small perturbation voltage injection source. Since this power source only has three-phase output terminals that can be connected to other components, the three-phase resistor load has to be serially connected between the power source and the MMC in this experiment. However, the resistor load does not affect the measured MMC impedance, because the converter-side voltage and current of the MMC are measured, from which the resulting perturbation voltage and current are extracted and the MMC impedance is then calculated by the ratio of the resulting perturbation voltage to current. In addition, since the programmable power source is merely used as a small perturbation voltage injection in this experiment, the output voltage of the programmable power source is set to be very low. The available output frequency range of the programmable power source is from 16 to 500 Hz. Furthermore, since the focus of this paper is on the low-frequency impedance characteristics of the MMC, the high resolution of frequency perturbation with an interval of 1 Hz was used below the 50 Hz frequency range, while an interval of 2 Hz in the frequency range of 50–100 Hz, an interval of 10 Hz in the frequency range of 100–200 Hz, and then the impedance responses at 250, 300, 400, and 500 Hz were also measured. A dc power source is connected to the dc terminals of the MMC. The schematic diagram of the experimental setup is illustrated in Fig. 19. The main electrical parameters of the experimental setup are as follows: dc voltage $V_{\rm dc} = 500\,\rm V$, ac phase voltage amplitude $V_m = 200\,\rm V$, SM number per arm $N = 12$, SM capacitance $C_{\rm SM} = 6.6\,\rm mF$, arm inductance $L = 5\,\rm mH$, load resistance $R_L = 10\,\Omega$, and output phase rms voltage of the programmable power source 7 V.

It is worth noting that there are relatively significant resistive components in the low-voltage MMC experimental setup, compared with the high-voltage applications. As a result, the internal damping of the low-voltage MMC setup is much stronger than that of the high-voltage one, which means that the instability issues caused by the internal dynamics of the MMC are not prominent for the low-voltage MMC setup. This is a key factor to be considered in order to simulate the actual operating characteristics of the high-voltage MMC setups. Therefore, a virtual resistance compensation (VRC)-based strategy is proposed in this work to counteract the actual physical resistance in order to make the operating characteristics of the low-voltage MMC setup appear closer to those of the high-voltage one. As aforementioned, the circulating current control strategy essentially increases the arm equivalent series resistance because of the positive proportional gain R_a. But if the proportional gain R_a is negative, it can be regarded as a negative resistance that can counteract the arm parasitic resistance. Therefore, the resistance compensation strategy based on the circulating current control with negative R_a in Fig. 6 is used in the course of impedance measurements on the MMC experimental setup, where the circulating current reference is the same as that with positive R_a, i.e., $i_{cx}^* = P/3/V_{\rm dc}$.

At first, the ac-side small-signal impedance of the MMC with open-loop control was measured in the case of no VRC control, as shown in Fig. 20, where it can be seen that there is a good agreement between the experimental measurement impedance and the analytical model. It is worth noting that there is no low-frequency resonance peak in the MMC impedance, which is due to the relatively large resistive components in the low-voltage MMC experimental setup. Furthermore, the analytical impedance is obtained by setting the arm resistance $R = 1\,\Omega$, which shows a good matching with the experimental results. It indicates that the equivalent arm resistance of the MMC experimental setup is approximately equal to 1 Ω. Since the effect of the circulating current control with positive R_a is similar to that of the physical arm resistance, the measurements for the MMC

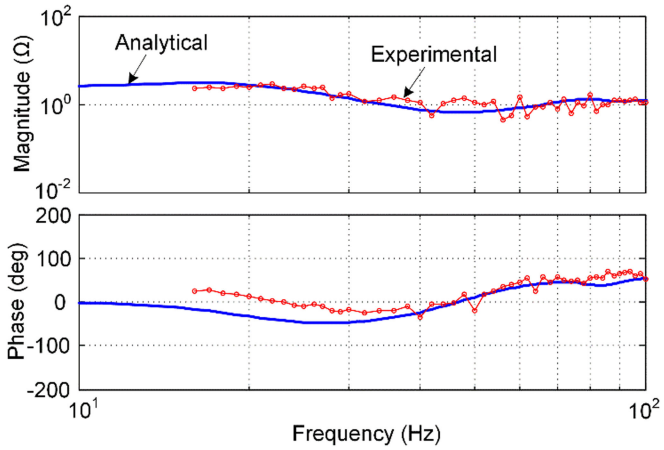

Fig. 20. Experimental measurement impedance with open-loop control and without VRC.

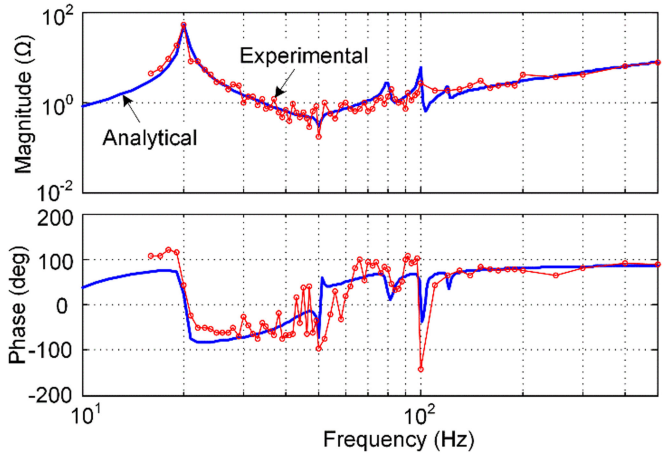

Fig. 22. Experimental measurement impedance with ac voltage closed-loop control and with VRC.

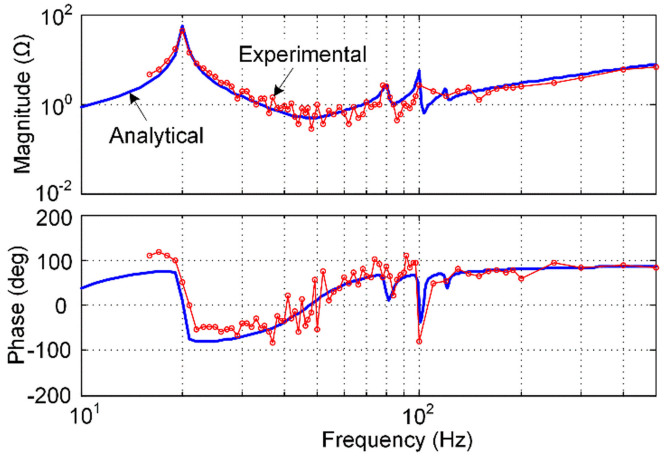

Fig. 21. Experimental measurement impedance with open-loop control and with VRC.

impedance under the circulating current control with positive R_a are no longer given in this paper.

Then, the ac-side small-signal impedances of the MMC with VRC control were measured in the experiments, as shown in Figs. 21 and 22, where the proportional gain $R_a = -1$. Figs. 21 and 22 are the comparisons between the analytical and experimentally measured impedances of the MMC with open-loop control and ac voltage closed-loop control, respectively. As can be seen, although there exist some errors at lower frequencies, the experimental measurements exhibit good overall matching to the analytical impedances. In addition, it is worth noting that the low-frequency resonance peaks appear in the MMC impedances when the resistance compensation strategy is used, which confirms the effectiveness of the proposed resistance compensation strategy.

It is noted that the differences between the experimental and analytical impedances in the low-frequency range (e.g., $<$150 Hz) are larger than those at higher frequencies, which can be attributed to two reasons. The first reason is that there are large background noises around fundamental frequency so that the injected perturbation signals at frequencies around fundamental frequency are difficult to be accurately extracted, even though having subtracted the original harmonic components in the voltage and current (before injecting the small perturbation) from the perturbed voltage and current (after injecting the small perturbation), since some exogenous frequency contents may be generated due to the nonlinear and nonideal components in the experimental setup. The second reason is due to the effect of the internal harmonic dynamics and interaction between harmonic components of arm and line quantities of the MMC, which could further affect the measurement results. Nevertheless, since the impedance characteristics of the MMC in the high-frequency range ($>$150 Hz) are inductive, which are dominated by the arm inductance, the MMC impedance can be regarded to be linear in the high-frequency range. Hence, there exist much less background harmonics or exogenous frequency contents in this frequency range so that the magnitudes and phase angles of the MMC impedance are easier to be accurately measured compared to the lower frequencies.

VI. Conclusion

This paper presents the small-signal impedance modeling of the MMC based on the HSS method. The HSS method is first used for the MMC modeling, which considers all the internal harmonics within the MMC. The steady-state and small-signal HSS models of the MMC are developed, based on which, the small-signal impedance of the MMC is then derived. The simulation and experimental results validate the proposed models. The results show that the MMC internal harmonics have a great impact on the terminal impedance of the MMC in the low-frequency range ($<$150 Hz). Furthermore, different control schemes are also considered to reveal the impact of the control on the MMC impedance. The proposed MMC impedance model has been used to analyze the stability of the MMC-HVDC-connected wind farm, which shows the feasibility of the proposed impedance model.

REFERENCES

[1] M. A. Perez, S. Bernet, J. Rodriguez, S. Kouro, and R. Lizana, "Circuit topologies, modeling, control schemes, and applications of modular multilevel converter," *IEEE Trans. Power Electron.*, vol. 30, no. 1, pp. 4–17, Jan. 2015.

[2] S. Dehnath, J. Qin, B. Bahrani, M. Saeedifard, and P. Barbosa, "Operation, control, and applications of the modular multilevel converter: A review," *IEEE Trans. Power Electron.*, vol. 30, no. 1, pp. 37–53, Jan. 2015.

[3] L. Harnefors, A. Antonopoulos, S. Norrga, L. Ängquist, and H. P. Nee, "Dynamic analysis of modular multilevel converters," *IEEE Trans. Ind. Electron.*, vol. 60, no. 7, pp. 2526–2537, Jul. 2013.

[4] K. Ilves, A. Antonopoulos, S. Norrga, and H. P. Nee, "Steady-state analysis of interaction between harmonic components of arm and line quantities of modular multilevel converters," *IEEE Trans. Power Electron.*, vol. 27, no. 1, pp. 57–68, Jan. 2012.

[5] X. Li, Q. Song, W. Liu, S. Xu, Z. Zhu, and X. Li, "Performance analysis and optimization of circulating current control for modular multilevel converter," *IEEE Trans. Ind. Electron.*, vol. 63, no. 2, pp. 716–727, Feb. 2016.

[6] J. Lv, P. Dong, G. Shi, X. Cai, H. Rao, and J. Chen, "Subsynchronous oscillation of large DFIG-based wind farms integration through MMC-based HVDC," in *Proc. Int. Conf. Power Syst. Technol.*, Chengdu, China, 2014, pp. 2401–2408.

[7] J. Lyu, X. Cai, and M. Molinas, "Frequency domain stability analysis of MMC-based HVdc for wind farm integration," *IEEE J. Emerging Sel. Topics Power Electron.*, vol. 4, no. 1, pp. 141–151, Mar. 2016.

[8] J. Lyu, X. Cai, and M. Molinas, "Optimal design of controller parameters for improving the stability of MMC-HVDC for wind farm integration," *IEEE J. Emerging Sel. Topics Power Electron.*, vol. 6, no. 1, pp. 40–53, Mar. 2018.

[9] D. Ludois and G. Venkataramanan, "Simplified terminal behavioral model for a modular multilevel converter," *IEEE Trans. Power Electron.*, vol. 29, no. 4, pp. 1622–1631, Apr. 2014.

[10] G. Bergna, J. A. Suul, and S. D'Arco, "Small-signal state-space modeling of modular multilevel converters for system stability analysis," in *Proc. IEEE Energy Convers. Congr. Expo.*, 2015, pp. 5822–5829.

[11] N. T. Trinh, M. Zeller, K. Wuerflinger, and I. Erlich, "Generic model of MMC-VSC-HVDC for interaction study with ac power system," *IEEE Trans. Power Syst.*, vol. 31, no.1, pp. 27–34, Jan. 2016.

[12] Y. Li *et al.*, "Modeling and damping control of modular multilevel converter based dc grid," *IEEE Trans. Power Syst.*, vol. 33, no. 1, pp. 723–735, Jan. 2018.

[13] D. Jovcic and A. A. Jamshidifar, "Phasor model of modular multilevel converter with circulating current suppression control," *IEEE Trans. Power Del.*, vol. 30, no. 4, pp. 1889–1897, Aug. 2015.

[14] A. Jamshidifar and D. Jovcic, "Small-signal dynamic DQ model of modular multilevel converter for system studies," *IEEE Trans. Power Del.*, vol. 31, no. 1, pp. 191–199, Feb. 2016.

[15] T. Li, A. M. Gole, and C. Zhao, "Harmonic instability in MMC-HVDC converters resulting from internal dynamics," *IEEE Trans. Power Del.*, vol. 31, no. 4, pp. 1738–1747, Aug. 2016.

[16] N. R. Chaudhuri, R. Oliveira, and A. Yazdani, "Stability analysis of vector-controlled modular multilevel converters in linear time-periodic framework," *IEEE Trans. Power Electron.*, vol. 31, no. 7, pp. 5255–5269, Jul. 2016.

[17] J. Wang, J. Liang, F. Gao, X. Dong, C. Wang, and B. Zhao, "A closed-loop time-domain analysis method for modular multilevel converter," *IEEE Trans. Power Electron.*, vol. 32, no. 10, pp. 7494–7508, Oct. 2017.

[18] N. M. Wereley and S. R. Hall, "Linear time periodic systems: Transfer function, poles, transmission zeroes and directional properties," in *Proc. Amer. Control Conf.*, Boston, MA, USA, Jun. 1991, pp. 1179–1184.

[19] J. Arrillaga, A. Medina, M. L. V. Lisboa, M. A. Cavia, and P. Sanchez, "The harmonic domain. A frame of reference for power system harmonic analysis," *IEEE Trans. Power Syst.*, vol. 10, no. 1, pp. 433–440, Feb. 1995.

[20] G. N. Love and A. R. Wood, "Harmonic state space model of power electronics," in *Proc. Int. Conf. Harmon. Qual. Power*, Wollongong, N.S.W., Australia, 2008, pp. 1–6.

[21] J. R. C. Orillaza and A. R. Wood, "Harmonic state-space model of a controlled TCR," *IEEE Trans. Power Del.*, vol. 28, no. 1, pp. 197–205, Jan. 2013.

[22] J. Kwon, X. Wang, F. Blaabjerg, C. L. Bak, V. S. Sularea, and C. Busca, "Harmonic interaction analysis in a grid-connected converter using harmonic state-space (HSS) modeling," *IEEE Trans. Power Electron.*, vol. 32, no. 9, pp. 6823–6835, Sep. 2017.

[23] J. Kwon, X. Wang, F. Blaabjerg, C. L. Bak, A. R. Wood, and N. R. Watson, "Harmonic instability analysis of a single-phase grid-connected converter using a harmonic state-space modeling method," *IEEE Trans. Ind. Appl.*, vol. 52, no. 5, pp. 4188–4200, Sep. 2016.

[24] J. Kwon, X. Wang, F. Blaabjerg, C. L. Bak, A. R. Wood, and N. R. Watson, "Linearized modeling methods of ac-dc converters for an accurate frequency response," *IEEE J. Emerging Sel. Topics Power Electron.*, vol. 5, no. 4, pp. 1526–1541, Dec. 2017.

[25] M. Esparza, J. S. Ramírez, J. Kwon, X. Wang, and F. Blaabjerg, "Modeling of VSC-based power systems in the extended harmonic domain," *IEEE Trans. Power Electron.*, vol. 32, no. 8, pp. 5907–5916, Aug. 2017.

[26] V. Salis, A. Costabeber, S. Cox, P. Zanchetta, and A. Formentini, "Stability boundary analysis in single-phase grid-connected inverters with PLL by LTP theory," *IEEE Trans. Power Electron.*, vol. 33, no. 5, pp. 4023–4036, Mar. 2018.

[27] J. Lyu, M. Molinas, and X. Cai, "Harmonic state space modeling of a three-phase modular multilevel converter," arXiv: 1706.09925 [cs.SY], Jun. 2017.

[28] J. Sun, "Impedance-based stability criterion for grid-connected inverters," *IEEE Trans. Power Electron.*, vol. 26, no. 11, pp. 3075–3078, Nov. 2011.

[29] B. Wen, D. Dong, D. Boroyevich, R. Burgos, P. Mattavelli, and Z. Shen, "Impedance-based analysis of grid-synchronization stability for three-phase paralleled converters," *IEEE Trans. Power Electron.*, vol. 31, no. 1, pp. 26–38, Jan. 2016.

[30] M. Cespedes and J. Sun, "Impedance modeling and analysis of grid-connected voltage-source converters," *IEEE Trans. Power Electron.*, vol. 29, no. 3, pp. 1254–1261, Mar. 2014.

[31] L. Harnefors, M. Bongiorno, and S. Lundberg, "Input-admittance calculation and shaping for controlled voltage-source converters," *IEEE Trans. Ind. Electron.*, vol. 54, no. 6, pp. 3323–3334, Dec. 2007.

[32] B. Wen, D. Boroyevich, R. Burgos, P. Mattavelli, and Z. Shen, "Analysis of D-Q small-signal impedance of grid-tied inverters," *IEEE Trans. Power Electron.*, vol. 31, no. 1, pp. 675–687, Jan. 2016.

[33] X. Shi, Z. Wang, B. Liu, Y. Li, L. M. Tolbert, and F. Wang, "DC impedance modeling of a MMC-HVDC system for dc voltage ripple prediction under a single-line-to-ground fault," in *Proc. IEEE Energy Convers. Congr. Expo.*, Pittsburgh, PA, USA, 2014, pp. 5339–5346.

[34] R. Mo, Q. Ye, and H. Li, "DC impedance modeling and stability analysis of modular multilevel converter for MVDC application," in *Proc. IEEE Energy Convers. Congr. Expo.*, Milwaukee, WI, USA, 2016, pp. 1–5.

[35] J. Lyu, X. Cai, and M. Molinas, "Impedance modeling of modular multilevel converters," in *Proc. Annu. Conf. IEEE Ind. Electron. Soc.*, Yokohama, Japan, 2015, pp. 180–185.

[36] M. Beza, M. Bongiorno, and G. Stamatiou, "Analytical derivation of the ac-side input admittance of a modular multilevel converter with open- and closed-loop control strategies," *IEEE Trans. Power Del.*, vol. 33, no. 1, pp. 248–256, Feb. 2018.

[37] J. Lyu, Q. Chen, and X. Cai, "Impedance modeling of modular multilevel converter by harmonic linearization," in *Proc. IEEE 17th Workshop Control Model. Power Electron.*, Trondheim, Norway, 2016, pp. 1–6.

[38] Q. Chen, J. Lyu, R. Li, and X. Cai, "Impedance modeling of modular multilevel converter based on harmonic state space," in *Proc. IEEE 17th Workshop Control Model. Power Electron.*, Trondheim, Norway, 2016, pp. 1–5.

[39] J. Sun and H. Chao, "Impedance modeling and analysis of modular multilevel converters," in *Proc. IEEE 17th Workshop Control Model. Power Electron.*, Trondheim, Norway, 2016, pp. 1–9.

Jing Lyu (S'14–M'16) received the B.Eng. degree from China University of Mining and Technology, Jiangsu, China, in 2009, and the M.Eng. and Ph.D. degrees from Shanghai Jiao Tong University, Shanghai, China, in 2011 and 2016, respectively, all in electrical engineering.

He was a Postdoctoral Research Fellow with the Department of Engineering Cybernetics, Norwegian University of Science and Technology, Trondheim, Norway, from 2016 to 2017. Since 2018, he has been a tenure-track Assistant Professor with the Department of Electrical Engineering, Shanghai Jiao Tong University. His current research interests include dynamic stability of modular multilevel converter (MMC)-based high-voltage direct current connected wind farms/photovoltaic plants, modeling and control of the MMC, dynamic modeling of wind turbines and wind farms, and impedance modeling.

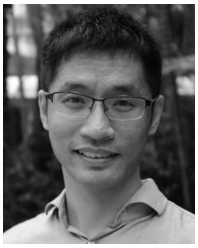

Xin Zhang (M'15) received the Ph.D. degree in automatic control and systems engineering from the University of Sheffield, Sheffield, U.K., in 2016, and the Ph.D. degree in electronic and electrical engineering from Nanjing University of Aeronautics and Astronautics, Nanjing, China, in 2014.

Currently, he is an Assistant Professor of power engineering with the School of Electrical and Electronic Engineering, Nanyang Technological University, Singapore. He was a Postdoctoral Research Fellow (Jan. 2017 to Sep. 2017) with the City University of Hong Kong and a Research Associate (Feb. 2014 to Dec. 2016) with the University of Sheffield. His general research interests include power electronics, power system, and advanced control theory, together with their applications in various sectors.

Dr. Zhang was a recipient of the highly prestigious Chinese National Award for Outstanding Students Abroad in 2016.

Xu Cai received the B.Eng. degree from Southeast University, Nanjing, China, in 1983, and the M.Eng. and Ph.D. degrees from China University of Mining and Technology, Jiangsu, China, in 1988 and 2000, respectively, all in electrical engineering.

He was with the Department of Electrical Engineering, China University of Mining and Technology, as an Associate Professor from 1989 to 2001. He was the Vice Director of the State Energy Smart Grid R&D Center, Shanghai, China, from 2010 to 2013. Since 2002, he has been a Professor with Shanghai Jiao Tong University, Shanghai, where he has also been the Director of the Wind Power Research Center since 2008. His current research interests include power electronics and renewable energy exploitation and utilization, including wind power converters, wind turbine control system, large power battery storage systems, clustering of wind farms and its control system, and grid integration.

Marta Molinas (M'94) received the Diploma degree in electromechanical engineering from the National University of Asuncion, Asuncion, Paraguay, in 1992, the M.Eng. degree from Ryukyu University, Nishihara, Japan, in 1997, and the D.Eng. degree from Tokyo Institute of Technology, Tokyo, Japan, in 2000.

She was a Guest Researcher with the University of Padova, Padova, Italy, in 1998. From 2004 to 2007, she was a Postdoctoral Researcher with the Norwegian University of Science and Technology (NTNU), Trondheim, Norway. From 2008 to 2014, she was a Professor with the Department of Electric Power Engineering, NTNU. She is currently a Professor with the Department of Engineering Cybernetics, NTNU. Her current research interests include stability of power electronics systems, harmonics, instantaneous frequency, and nonstationary signals from the human and the machine.

Dr. Molinas is an Associate Editor for the IEEE JOURNAL OF EMERGING AND SELECTED TOPICS IN POWER ELECTRONICS, the IEEE TRANSACTIONS ON POWER ELECTRONICS (IEEE PELS), and the IEEE TRANSACTIONS ON INDUSTRIAL ELECTRONICS, and an Editor for the IEEE TRANSACTIONS ON ENERGY CONVERSION. She is a member of the committee of the IEEE PELS Humanitarian Initiative Billion Smiles. She has been an AdCom Member of the IEEE Power Electronics Society from 2009 to 2011.